upper layers are lost, the star would be left with an O/Ne/Mg envelope (an oxygen-neon white dwarf), as we observe. For the complete removal of the H/He/C envelope, a late C-shell flash, strong mass loss, and/or close binary evolution, including mergers of white dwarfs, are possible scenarios. That several different scenarios for the late evolution might be needed is also suggested by the discussion of progenitor types and evolutionary paths observed in type Ia supernovae (*26*–*29*).

Distinct from hot pre–white dwarfs with oxygen lines (*4*) and cool oxygen line spectra white dwarfs (*10*, *11*), which have C and He rich atmospheres, we have found a star with oxygen 25 times more abundant than any other element, by number, the only one known among the roughly 32,000 SDSS white dwarf stars (*13*). Time-series spectroscopy of the object will be required to search for a close binary companion, which could point toward the evolutionary path of such a rare object.

REFERENCES AND NOTES

1. X. Meng, X. Chen, Z. Han, *Astron. Astrophys.* **487**, 625–635 (2008).
2. A. D. Romero, F. Campos, S. O. Kepler, *Mon. Not. R. Astron. Soc.* **450**, 3708–3723 (2015).
3. E. Schatzman, *Nature* **161**, 61–62 (1948).
4. K. Werner, T. Rauch, *Astron. Astrophys.* **584**, A19 (2015).
5. P. Dufour, G. Fontaine, J. Liebert, G. D. Schmidt, N. Behara, *Astrophys. J.* **683**, 978–989 (2008).
6. P. Dufour, in *White Dwarf Atmospheres and Circumstellar Environments*, D. W. Hoard, Ed. (Wiley-VCH, 2011), pp. 53–88.
7. D. Koester, J. Provencal, B. T. Gänsicke, *Astron. Astrophys.* **568**, A118 (2014).
8. B. Dunlap, J. C. Clemens, in *19th European Workshop on White Dwarfs*, P. Dufour, P. Bergeron, G. Fontaine, Eds., Astronomical Society of the Pacific Conference Series, **493**, 547 (2015).
9. J. Liebert *et al.*, *Astron. J.* **126**, 2521–2528 (2003).
10. B. T. Gänsicke, D. Koester, J. Girven, T. R. Marsh, D. Steeghs, *Science* **327**, 188–190 (2010).
11. S. O. Kepler *et al.*, *Mon. Not. R. Astron. Soc.* **446**, 4078–4087 (2015).
12. S. Alam *et al.*, *Astrophys. J. Suppl. Ser.* **219**, 12 (2015).
13. S. O. Kepler *et al.*, *Mon. Not. R. Astron. Soc.* **455**, 3413–3423 (2016).
14. L. Bianchi, A. Conti, B. Shiao, *Adv. Space Res.* **53**, 900–912 (2014).
15. L. G. Althaus *et al.*, *Astrophys. J.* **704**, 1605–1615 (2009).
16. L. Barrón-Palos *et al.*, *Nucl. Phys. A.* **779**, 318–332 (2006).
17. E. Garcia-Berro, I. Iben, *Astrophys. J.* **434**, 306 (1994).
18. K. Nomoto, C. Kobayashi, N. Tominaga, *Annu. Rev. Astron. Astrophys.* **51**, 457–509 (2013).
19. K. Nomoto, in *Supernova Environmental Impacts*, A. Ray, R. A. McCray, Eds., vol. 296 of *Proceedings of the International Astronomical Union* (2014), pp. 27–36.
20. C. L. Doherty *et al.*, *Mon. Not. R. Astron. Soc.* **441**, 582–598 (2014).
21. C. L. Doherty, P. Gil-Pons, H. H. B. Lau, J. C. Lattanzio, L. Siess, *Mon. Not. R. Astron. Soc.* **437**, 195–214 (2014).
22. P. A. Denissenkov *et al.*, *Mon. Not. R. Astron. Soc.* **447**, 2696–2705 (2015).
23. M. C. Chen, F. Herwig, P. A. Denissenkov, B. Paxton, *Mon. Not. R. Astron. Soc.* **440**, 1274–1280 (2014).
24. J. D. Cummings, J. S. Kalirai, P.-E. Tremblay, E. Ramirez-Ruiz, Two massive white dwarfs from NGC 2323 and the initial-final mass relation for progenitors of 4 to 6.5 $M_{\odot}$, http://arxiv.org/abs/1601.03053 (2016).
25. F. Herwig, T. Blöcker, N. Langer, T. Driebe, *Astron. Astrophys.* **349**, L5 (1999).
26. C. L. Fryer *et al.*, *Astrophys. J.* **725**, 296–308 (2010).
27. R. Pakmor *et al.*, *Nature* **463**, 61–64 (2010).
28. K. J. Shen, D. Kasen, N. N. Weinberg, L. Bildsten, E. Scannapieco, *Astrophys. J.* **715**, 767–774 (2010).
29. M. Dan, S. Rosswog, J. Guillochon, E. Ramirez-Ruiz, *Mon. Not. R. Astron. Soc.* **422**, 2417–2428 (2012).

ACKNOWLEDGMENTS

D.K. is supported by Science without Borders, Ministério de Ciência Tecnologia e Inovação/Ministério da Educação-Brazil. Funding for SDSS-III has been provided by the Alfred P. Sloan Foundation, the Participating Institutions, the National Science Foundation, and the U.S. Department of Energy Office of Science. The SDSS-III web site is www.sdss3.org. SDSS-III is managed by the Astrophysical Research Consortium for the Participating Institutions of the SDSS-III Collaboration, including the University of Arizona, the Brazilian Participation Group, Brookhaven National Laboratory, Carnegie Mellon University, University of Florida, the French Participation Group, the German Participation Group, Harvard University, the Instituto de Astrofísica de Canarias, the Michigan State/Notre Dame/Joint Institute for Nuclear Astrophysics Participation Group, Johns Hopkins University, Lawrence Berkeley National Laboratory, Max Planck Institute for Astrophysics, Max Planck Institute for Extraterrestrial Physics, New Mexico State University, New York University, Ohio State University, Pennsylvania State University, University of Portsmouth, Princeton University, the Spanish Participation Group, University of Tokyo, University of Utah, Vanderbilt University, University of Virginia, University of Washington, and Yale University. The spectrum can be downloaded at http://dr12.sdss3.org/sas/dr12/sdss/spectro/redux/v5_7_0/spectra/7120/spec-7120-56720-0894.fits and the SDSS photometry from http://skyserver.sdss.org/dr7/en/tools/explore/obj.asp?ra=12%2040%2043.01&dec=+67%2010%2034.68.

SUPPLEMENTARY MATERIALS

www.sciencemag.org/content/352/6281/67/suppl/DC1
Supplementary Text
Tables S1 to S11
Model Spectrum
References (*30*–*45*)

18 October 2015; accepted 19 February 2016
10.1126/science.aad6705

COLLOIDAL ORDERING

Triclinic nematic colloidal crystals from competing elastic and electrostatic interactions

Haridas Mundoor,[1] Bohdan Senyuk,[1] Ivan I. Smalyukh[1,2,3]*

The self-assembly of nanoparticles can enable the generation of composites with predesigned properties, but reproducing the structural diversity of atomic and molecular crystals remains a challenge. We combined anisotropic elastic and weakly screened electrostatic interactions to guide both orientational and triclinic positional self-ordering of inorganic nanocrystals in a nematic fluid host. The lattice periodicity of these low-symmetry colloidal crystals is more than an order of magnitude larger than the nanoparticle size. The orientations of the nanocrystals, as well as the crystallographic axes of the ensuing triclinic colloidal crystals, are coupled to the uniform alignment direction of the nematic host, which can be readily controlled on large scales. We examine colloidal pair and many-body interactions and show how triclinic crystals with orientational ordering of the semiconductor nanorods emerge from competing long-range elastic and electrostatic forces.

Since Einstein's seminal work on Brownian motion and Perrin's subsequent experiments (*1*), which showed that particles in colloidal dispersions obey the same statistical thermodynamics as atoms, the colloid-atom analogy has provided insights into the physics of atomic systems through its application in studies exploring the dynamics of colloidal crystals and glasses (*2*). This analogy has inspired the development of forms of self-assembly that attempt to reproduce the diversity of atomic crystals (*3*), although experimental realization of colloidal architectures with low symmetry, such as triclinic systems, remains challenging. At the same time, the self-assembly of colloids can be designed and controlled by exploiting aspects of particle shape (*4*) and topology (*5*), the dispersing medium's anisotropy (*6*) and composition (*7*), DNA functionalization and origami-like designs (*8*), and the facile response of particles and media to external fields (*9*, *10*). Long-range interactions are of special interest, because they can lead to the sparse but ordered assembly of colloidal composites with unusual physical behavior (*9*). Long-range electrostatic repulsions in fluids with low ionic strength (*10*–*13*) have been used to obtain crystals and plastic crystals with high-symmetry colloidal lattices. These electrostatic interactions remain relatively isotropic at large separations, despite anisotropic particles shapes (*10*). In nematic liquid crystal (NLC) hosts, highly anisotropic long-range colloidal interactions arise from the minimization of free energy associated with particle-induced elastic distortions of the NLC molecular alignment, even when particles are spherical (*6*, *14*–*16*), although the ability to control the shape of particles provides a means of

[1]Department of Physics and Soft Materials Research Center, University of Colorado, Boulder, CO 80309, USA.
[2]Department of Electrical, Computer, and Energy Engineering, Materials Science and Engineering Program, University of Colorado, Boulder, CO 80309, USA.
[3]Renewable and Sustainable Energy Institute, National Renewable Energy Laboratory and University of Colorado, Boulder, CO 80309, USA.
***Corresponding author. E-mail: ivan.smalyukh@colorado.edu**

guiding self-assembly (*17*). The diversity of elastic interactions, which commonly resembles that of electrostatic dipolar and quadrupolar charge distributions (*6*, *14*, *17*), has enabled colloidal self-assembly of lamellae and dipolar crystals (*18*, *19*), although the interparticle spacing in these lamellar and crystalline assemblies could be controlled only within a range comparable to the particle sizes.

We demonstrate that competition between long-range electrostatic and elastic interactions leads to a highly unusual self-organization of rod-like nanoparticles that exhibits both long-range orientational and triclinic positional ordering. The micrometer-range colloidal crystal lattice parameters of these assemblies, as revealed by three-dimensional (3D) optical imaging, are an order of magnitude larger than the size of the constituent colloidal semiconductor nanorods (30 × 150 nm; fig. S1). We characterized pair interactions between nanorods and the structure and dynamics of their dispersions at different surface charges and volume fractions. Although various dislocations, grain boundaries, vacancies, and other defects are observed in these "soft" crystals, the crystallographic axes of triclinic lattices and colloidal nanorods tend to follow the direction of the alignment of rod-like molecules of the NLC host fluid. This preferred orientation of rod-like molecules is dubbed the "director" $\mathbf{n}$, which can be controlled on large scales by using approaches similar to those used to manufacture displays. The mechanical coupling between the orientations of the nanorods, the lattice, and the director is due to elastic free-energy minimization at well-defined nanorod and triclinic colloidal crystal orientations relative to a far-field director $\mathbf{n}_0$ and confining surfaces; it thus has the potential to enable device-scale self-assembly of tunable composites.

Semiconductor nanorods with the composition β-$NaY_{0.5}Gd_{0.3}Yb_{0.18}Er_{0.02}F_4$, engineered to have rod-like geometric shapes and polarized up-conversion–based luminescence properties (Fig. 1 and fig. S1), were synthesized using a hydrothermal method (*20*–*23*). The dispersion of nanorods in the NLC host (*9*, *21*) was facilitated by surface functionalization of as-synthesized particles (*20*–*23*). In a typical process, 6 mg of initially oleic acid–capped nanorods in 8 ml of cyclohexane were added to 4 ml of deionized water with a small amount of hydrochloric acid to yield a pH of ~4, then stirred for 2 hours. During this process, oleic acid ligands became protonated and mixed with cyclohexane, leaving bare uncapped nanorods with positive surface charges (*21*–*23*). The nanorods were then washed with acetone four to five times, redispersed in water, and subsequently coated with methoxy-poly(ethylene glycol)silane (Si-PEG) (*21*). Typically, 5 mg of Si-PEG dissolved in 1 ml of ethanol was mixed with 5 ml of nanorod dispersion in deionized water (pH ~4) and stirred for 2 hours. After the reaction, particles were precipitated by centrifugation, dispersed in ethanol, and then redispersed in a pentylcyanobiphenyl (5CB) NLC host via mixing and subsequent solvent evaporation at an elevated temperature of 70°C; the NLC composite was then quenched to room temperature while vigorously stirring (*9*, *21*). NLC dispersions of nanorods were infiltrated into glass cells by means of capillary action. For planar boundary conditions for $\mathbf{n}$, inner surfaces of cell substrates were coated with aqueous polyvinyl alcohol (1 weight %) and rubbed unidirectionally. The cell gap thickness within 15 to 60 μm was set using Mylar films. The surface charging of particles was characterized by probing their electrophoretic mobility within the aligned NLC cell under an electric field that was applied to in-plane electrodes (fig. S2). We controlled the effective positive surface charge per nanorod within $Z^*e \approx +(60 \text{ to } 250)e$ (*22*), the Debye screening length ξ_D in the nonpolar 5CB within 0.1 to 1.2 μm, and the nanorods' surface

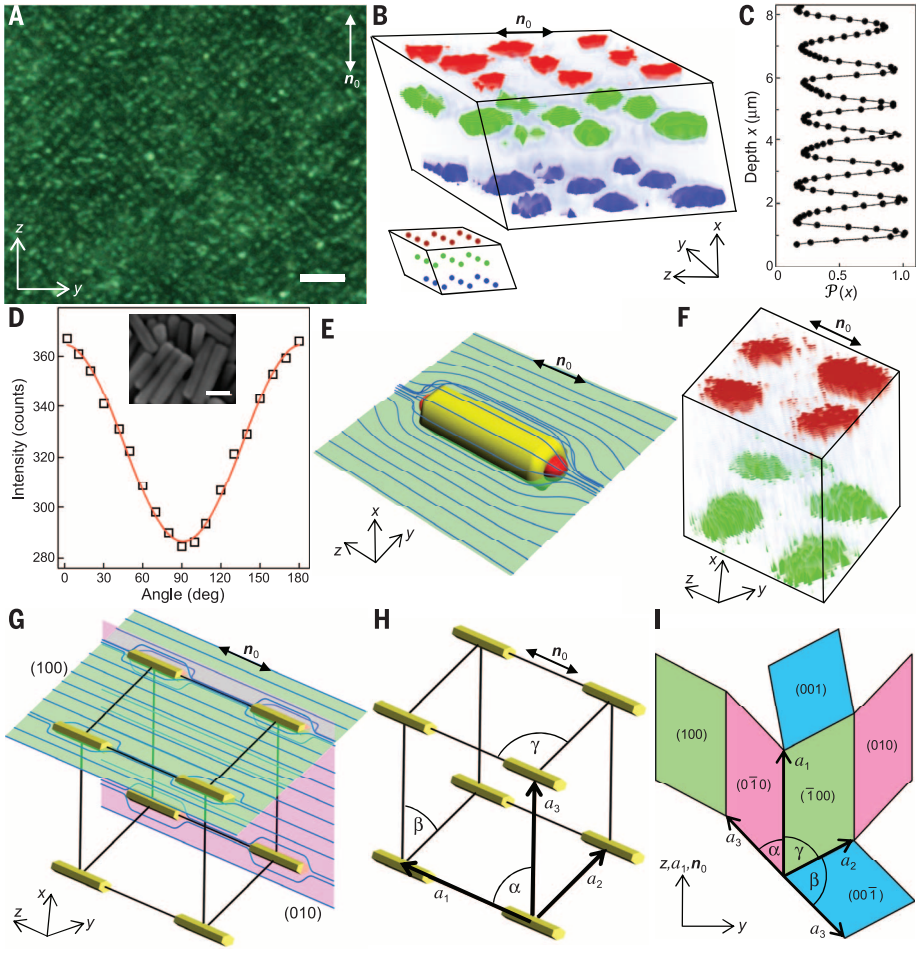

Fig. 1. Triclinic crystal self-assembly of nanorods in a NLC host. (**A**) Dark-field micrograph of a crystal assembly with lattice parameters a_1 = 1.30 ± 0.05 μm and a_2 = 1.01 ± 0.05 μm (scale bar, 5 μm). (**B**) 3D micrograph showing luminescence from a small part of a triclinic colloidal crystal, which was reconstructed from slow confocal microscopy scanning (obtained within ~3 min). It shows nanorod arrangements as they sense the potential energy landscape near their minimum-energy lattice sites. The luminescence signals from individual nanorods are shown in red, green, and blue to illustrate the locations of particles in three consecutive planes parallel to confining glass substrates. The bottom inset shows center-of-mass positions of building blocks in a triclinic crystal with the same lattice. The lattice parameters, based on averaging 18 independent local measurements, are as follows: a_1 = 1.49 ± 0.06 μm, a_2 = 0.95 ± 0.05 μm, a_3 = 1.20 ± 0.05 μm, α = 58° ± 2°, β = 69° ± 2°, and γ = 49° ± 2° [the angles α, β, and γ are defined in (H)]. (**C**) Probability ($\mathcal{P}$) distribution for finding nanorods at a depth x in the sample, relative to the center of the first colloidal layer parallel to the substrates (where x = 0). This distribution was calculated based on 3D luminescence imaging. (**D**) Luminescence intensity at 552 nm versus analyzer rotation between 0° and 180°. The inset shows a scanning electron microscopy image of the nanorods (scale bar, 50 nm). (**E**) Schematic illustration of director distortions (blue) around a single nanorod (yellow), with the red hemispheres at the poles depicting two particle-induced boojums. These quadrupolar elastic distortions are axially symmetric with respect to the nanorod axis (parallel to $\mathbf{n}_0$) and have mirror symmetry planes both parallel and orthogonal to $\mathbf{n}_0$. (**F**) 3D micrograph showing a primitive unit cell of a triclinic colloidal crystal, which was reconstructed from confocal scanning. Coloring is as in (B). (**G** to **I**) Schematics (not to scale) of a primitive cell of a triclinic colloidal crystal, (G) showing local director distortions (blue lines) induced by nanorods, (H) defining the parameters of a triclinic lattice, and (I) showing the lattice unfolded.

potential $\Phi_0 = Z^* e\xi_D/[\varepsilon_0\varepsilon(\Omega_{nr} + 4\pi l_{nr}\xi_D)]$ (*13*) within 28 to 129 mV; here, Z^* is an effective number of elementary charges $e = 1.6 \times 10^{-19}$ C, and Ω_{nr}, l_{nr}, ε, and ε_0 are the nanorod surface area, nanorod length, average dielectric constant of 5CB, and vacuum permittivity, respectively (*22*).

Dark-field and polarizing optical microscopies show the positional ordering of nanorods (Fig. 1A) and NLC alignment along $\mathbf{n}_0$ (fig. S3). The background-free 3D distribution of confocal luminescence from the nanorods, derived from an up-conversion process and collected while slowly scanning an infrared excitation laser beam (*22*), reveals colloidal crystals (Fig. 1, B, C, and F). During this 3D imaging, the nanorods sense the potential landscape and jiggle around their minimum-energy triclinic lattice sites (Fig. 1B). To investigate the orientations of nanorods within the lattice, we measured luminescence intensity while rotating the analyzer with respect to $\mathbf{n}_0$ (Fig. 1D). At all studied concentrations, the intensity of emission at 552 nm was greatest when the analyzer was parallel to $\mathbf{n}_0$, indicating that the nanorods align along $\mathbf{n}_0$ (fig. S1), as schematically depicted in Fig. 1E. This nanorod orientation is consistent with minimization of the total bulk elastic and surface anchoring free energy of NLCs around PEG-functionalized nanoparticles (*9*). Weak quadrupolar particle-induced elastic distortions are present in the NLC bulk, and the director orientation at the nanorod surfaces is compliant with tangential boundary conditions,

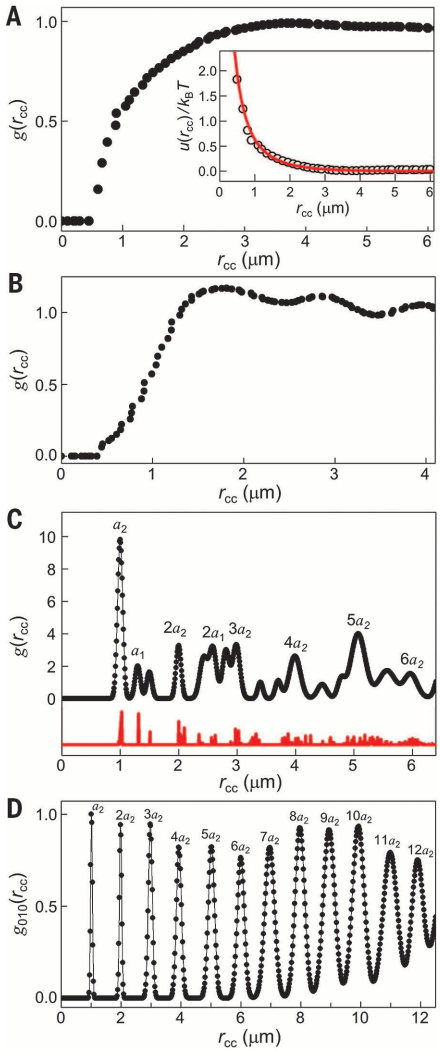

Fig. 2. Ordering of nanorods in 5CB. (**A**) Radial distribution function $g(r_{cc})$ for nanorod dispersion in the isotropic phase, consistent with the presence of long-range, repulsive, weakly screened electrostatic interactions. The inset shows pair potentials extracted from these data and fit by a screened Coulomb interactions potential (k_B, the Boltzmann constant; T, an absolute temperature) (*22*). (**B** and **C**) $g(r_{cc})$ for nanorod dispersion in the nematic phase at (B) a low ρ_N of ~0.35 μm^{-3} and (C) a high ρ_N of ~4.5 μm^{-3}, with emergent triclinic crystal ordering in the latter case. The normalized $g(r_{cc})$ (red) in (C) was calculated for the (100) plane of an ideal triclinic lattice with average dimensions determined from experiments; it serves as a visual guide for the corresponding experimental peaks. (**D**) Probability distribution $g_{010}(r_{cc})$, calculated for the experimental triclinic lattice along a_2 by averaging data for the [010] and [0$\bar{1}$0] directions. Numbers above the peaks indicate distances corresponding to integer numbers of lattice parameters a_1 and a_2.

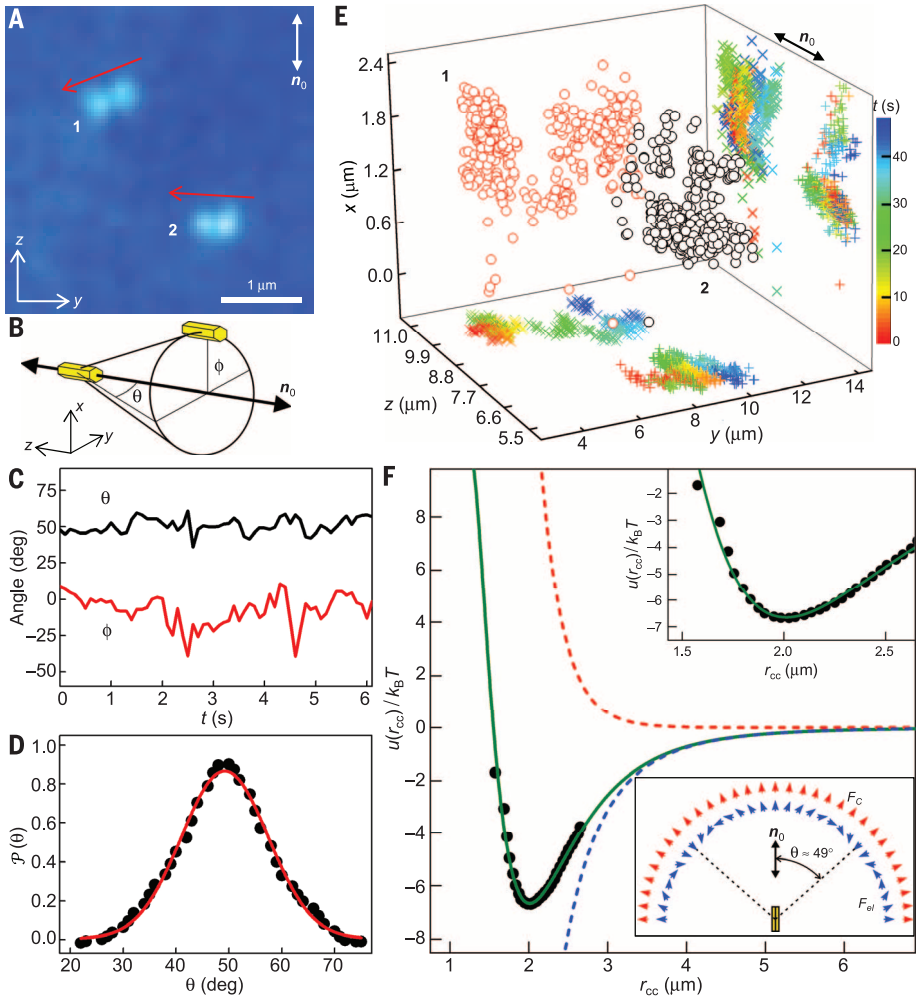

Fig. 3. Pair interactions between nanorods. (**A**) A representative DHPSF micrograph showing nanorods in 5CB at different depths of the cell, corresponding to different orientations of bright-lobe pairs 1 and 2 (marked by red arrows) (*25*). (**B**) Schematic of two nanorods with $\mathbf{r}_{cc}$ tilted with respect to $\mathbf{n}_0$ and the substrates, as characterized by angles θ and ϕ. (**C**) Typical changes in θ and ϕ over time t. (**D**) Probability distribution for measured θ; the red line is a Gaussian fit. (**E**) 3D positions of two nanorods over time, characterized with ≤10-nm precision and depicted by red (nanorod 1) and black (nanorod 2) open circles. The positions are shown projected onto the zx and zy planes, in which corresponding symbols × (nanorod 1) and + (nanorod 2) are colored according to the elapsed time. (**F**) Pair interaction potentials extracted from experimental data and fit with the sum of screened electrostatic and elastic potentials (green line). Dashed lines represent the electrostatic repulsive (red) and elastic attractive (blue) potentials. The top inset shows a close-up view near the potential well minimum. The bottom inset shows how the directions of the elastic force F_{el} (blue arrows) and screened Coulomb electrostatic repulsion force F_C (red arrows) depend on the angle between $\mathbf{r}_{cc}$ and $\mathbf{n}_0$.

except for the small surface point defect regions of discontinuity in the director field at the particle's poles, dubbed "boojums." By combining the nanorod orientation and position data, we experimentally identified a primitive lattice cell, based on confocal luminescence distributions from eight representative nanorods (Fig. 1F), and then reconstructed a triclinic pinacoidal lattice (Fig. 1, G to I), which allows for only the center inversion symmetry operation (*24*).

By examining nanorod displacements over time with video microscopy in dark-field and upconversion luminescence modes, we obtained the viscous drag coefficients (fig. S4) and the radial distribution function $g(r_{cc})$ (where r_{cc} is a center-to-center separation between nanorods) in both nematic and elevated-temperature isotropic phases (Fig. 2). Purely repulsive, direction-independent interactions are evident in the isotropic phase of the nematic host at 40°C (Fig. 2A). Once the host is cooled to the nematic phase at 28°C, $g(r_{cc})$ reveals attractive forces in both dilute and concentrated dispersions (Fig. 2, B and C). To explore the pair interactions between nanorods, we studied the trajectories of two particles that were brought close to each other with optical tweezers and then released (*22*). We used double-helix point spread function (DHPSF) microscopy (Fig. 3) (*22*, *25*) to find the 3D positions of nanorods within the cell over time with 7- to 10-nm precision (*25*), as well as to characterize the corresponding orientations of their center-to-center separation vector $\mathbf{r}_{cc}$ relative to $\mathbf{n}_0$. The nanorods equilibrate at micrometer-scale pair separations and with $\mathbf{r}_{cc}$ tilting away from the sample plane while circumscribing a cone of $\theta \approx 49° \pm 4°$ around $\mathbf{n}_0$; this would be impossible to quantify in 3D without DHPSF (Fig. 3, A to E). The pair interaction forces are highly anisotropic and long-ranged, and the angular distribution of $\mathbf{r}_{cc}$ orientations is consistent with the cone of maximum-attraction angles expected for colloidal elastic quadrupoles (Fig. 3) (*14*–*16*). Particle tracking gives the anisotropic distribution of nanorod displacements within equal intervals of elapsed time and gives the pair-interaction potential with a well-pronounced energetic minimum (Fig. 3F). Because the attractive van der Waals forces between nanorods are negligible at the relevant $\mathbf{r}_{cc}$ (*2*, *22*, *26*)—which is consistent with the fact that only repulsions persist when the host is heated to the isotropic phase (Fig. 2A)—we attribute this minimum in pair-interaction energy to the competition of elastic and electrostatic interactions. Considering the classical use of multipolar expansions in both nematic elasticity and electrostatics (*1*, *2*, *14*), we used their leading terms (i.e., a monopole for electrostatics, because of the surface charging of nanorods, and a quadrupole for nematic elasticity, because of the director distortions shown in Fig. 1E) to model these interactions. The total potential can be approximately described as a superposition $u \approx u_C + u_{el}$ of the quadrupolar elastic (u_{el}) and the electrostatic screened Coulomb (u_C) interaction potentials (*2*, *22*, *27*). This yields $u(r_{cc}) = (A_1/r_{cc})\exp(-r_{cc}/\xi_D) + A_2(9 - 90\cos^2\theta + 105\cos^4\theta)r_{cc}^{-5}$, where A_1 and A_2 are fitting parameters that are dependent on the size and charging of nanorods and on alignment, elastic, and dielectric properties (*22*). This expression fits well the distance dependence of the experimental potential (Fig. 3F) and explains the equilibrium orientation of $\mathbf{r}_{cc}$ at $\theta \approx 49° \pm 4°$ to $\mathbf{n}_0$. The Debye screening length $\xi_D = 0.34$ μm, derived from A_1 in $u(r_{cc})$ (*22*), matches the ξ_D that was independently obtained from fitting the repulsive electrostatic potential in the isotropic phase of 5CB, in which elastic forces vanish (inset of Fig. 2A). The strength of the elastic quadrupole moment derived from A_2 and the corresponding material parameters, such as elastic constants and anchoring coefficients, are consistent with theories of quadrupolar elastic interactions and independent experimental measurements (*14*–*16*, *22*).

As the concentration of nanorods increases, they exhibit gas-, liquid- and glass-like structural organizations, and crystalline order (Fig. 1 and figs. S5 to S7) emerges at concentrations that are roughly consistent with the average equilibrium separations in colloidal pairs and lattices (Figs. 1 to 3). Within the (100) crystallographic planes (Figs. 1 and 4A and table S1), $\mathbf{r}_{cc}$ tends to align at angles of ~49° to $\mathbf{n}_0$, similar to the orientation of the center-to-center separation vector of pairs of nanorods. By analyzing particle displacement distributions associated with different lattice sites in the triclinic colloidal crystal (Fig. 4B), we gained insight into the corresponding energy landscape (Fig. 4C) and obtained the average spring constant of the crystal, $k \approx 0.63$ pN μm^{-1}. Translational order in our triclinic lattices (Fig. 1A) is quantified by $g(r_{cc})$ (Fig. 2C) and the one-dimensional probability distribution function $g_{010}(r_{cc})$ (Fig. 2D), which is calculated along the direction of crystallographic axis a_2 (Fig. 1, H and I). We characterized the two-dimensional mean square displacement (MSD, $\langle\Delta r^2\rangle$) of the nanorods as a function of time t (Fig. 4D, inset). We then used it to estimate the so-called Lindemann parameter $\delta L = [3\langle\Delta r^2(t \to \infty)\rangle/4r_{nn}^2]^{1/2}$, where r_{nn} is the crystal nearest-neighbor equilibrium distance and $\langle\Delta r^2(t \to \infty)\rangle$ is the asymptotic value of the time-dependent MSD $\langle\Delta r^2(t)\rangle$ used for the estimate. This parameter is commonly used to characterize crystallization and melting transitions in terms of the MSD of particles around their ideal lattice positions, as compared with their nearest-neighbor distance. Plotting the Lindemann parameter against the nanorod number density ρ_N (Fig. 4D) shows

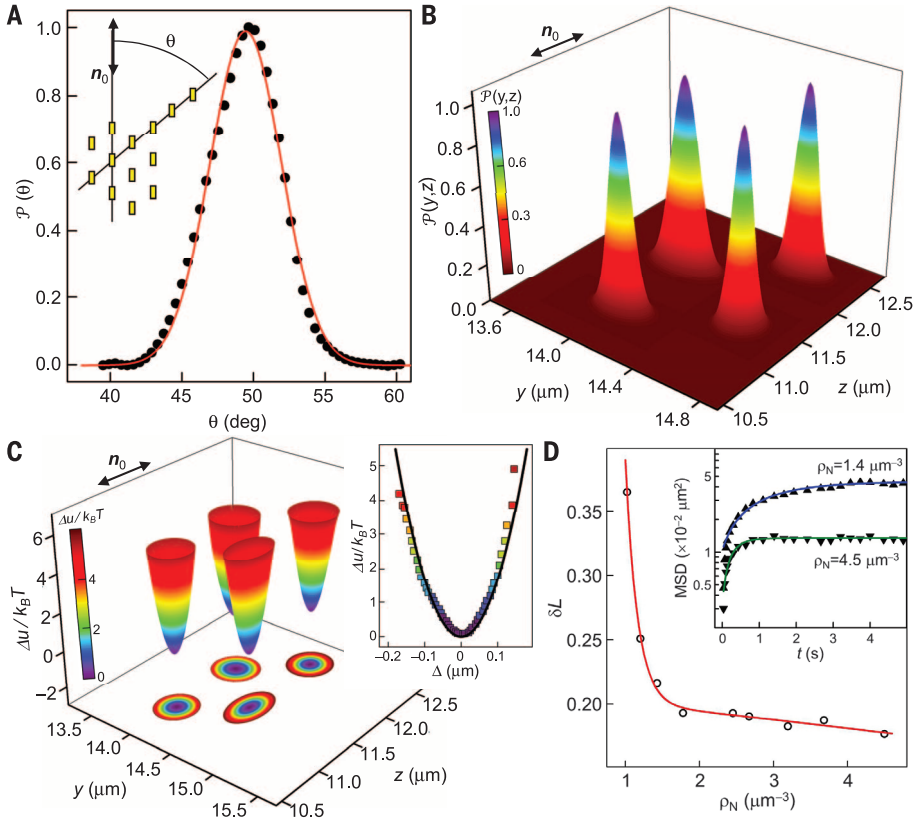

Fig. 4. Characterization of triclinic colloidal crystals. (**A**) Probability distribution of an angle θ (inset; yellow rectangles represent nanorods) measured in the (100) plane of a colloidal crystal. Its Gaussian fit is shown in red. (**B**) Probability distributions of positions within four lattice sites in the (100) plane of a triclinic crystal and (**C**) the corresponding potential landscape. The inset in (C) shows a dependence of the relative potential energy experienced by nanorods on local distance Δ. (**D**) Lindemann parameter δL versus nanorod number density ρ_N. The inset shows MSDs of nanorods over time t at $\rho_N = 1.4$ μm^{-3} (upright triangles) and 4.5 μm^{-3} (inverted triangles).

that its concentration-dependent behavior and values correspond to a crystallization transition that is consistent with that found in other condensed matter systems (*28*). A thermal expansion of ~0.01°C^{-1} of the lattice (fig. S8) stems from the decrease of an average NLC elastic constant K and quadrupolar elastic forces as temperature increases (K decreases by a factor of ~3 when the composite is heated from room temperature to ~34°C) (*22*).

Nanorods can be electrically concentrated and ordered starting from dilute initial dispersions (fig. S9), similar to the crystallization of hard sphere–like colloids when subjected to electrophoretic or dielectrophoretic forces (*29*). The triclinic crystal order is facilitated by applying 300 to 900 mV to transparent electrodes on inner substrates of the cell, which is lower than the threshold voltage needed for NLC switching. In response to these dc fields, the positively charged nanorods slowly move toward a negative electrode as a result of electrophoresis and eventually form a crystal as their concentration uniformly increases (fig. S9). These low voltages also facilitate uniform alignment of crystalline nuclei and healing of defects; in addition, they induce a giant electrostriction of the triclinic lattice, with ~25% strain at fields of 0.03 V μm^{-1} (fig. S8B). Because NLC is switched at ~1 V (*9*, *21*), colloidal crystal lattice orientations can be reconfigured while following the rotation of the director, although these processes are slow and complex. Electric fields, confinement in thin cells (thicknesses ≤15 μm) that are incompatible with an integer number of primitive cells in the colloidal crystal, variations in nanorod concentrations that exceed the range accommodated by an equilibrium triclinic lattice, and temperature changes control the primitive cell parameters (table S1) and prompt the formation of defects ranging from edge dislocations (fig. S11) to vacancies and grain boundaries (*2*, *22*, *30*).

We have introduced a highly tunable and reconfigurable colloidal system with competing long-range elastic and electrostatic interactions that lead to triclinic pinacoidal lattices of orientationally ordered nanorods. This unexpected triclinic crystallization of semiconductor particles at packing factors <<1% shows potential for the self-assembly of a wide variety of mesostructured composites on device-relevant scales, which can be tuned by weak external stimuli such as low-voltage fields and very small temperature changes. The control of particle charging allowed for tuning of the triclinic lattice periodicity between 0.5 and 1.6 μm, a range which can be extended by tuning the strength of electrostatic interactions through doping or deionizing NLCs (*10*–*13*) or through using nematics with different properties. Considering that dipolar and other multipolar elastic colloidal interactions in NLCs can be introduced and guided by controlling the boundary conditions at particle surfaces, and given that the control of NLC elastic constants may alter the angular dependencies of these interactions (*22*), our study sets the stage for explorations of mesoscopic colloidal positional and orientational ordering that can enable the engineering of material properties through spontaneous ordering of nanoparticles.

REFERENCES AND NOTES

1. H. N. W. Lekkerkerker, R. Tuinier, *Colloids and the Depletion Interaction* (Springer Netherlands, 2011).
2. P. M. Chaikin, T. C. Lubensky, *Principles of Condensed Matter Physics* (Cambridge Univ. Press, 1995).
3. V. N. Manoharan, *Science* **349**, 1253751 (2015).
4. P. F. Damasceno, M. Engel, S. C. Glotzer, *Science* **337**, 453–457 (2012).
5. B. Senyuk *et al.*, *Nature* **493**, 200–205 (2013).
6. P. Poulin, H. Stark, T. C. Lubensky, D. A. Weitz, *Science* **275**, 1770–1773 (1997).
7. S. Sacanna, W. T. M. Irvine, P. M. Chaikin, D. J. Pine, *Nature* **464**, 575–578 (2010).
8. M. R. Jones *et al.*, *Nat. Mater.* **9**, 913–917 (2010).
9. Q. Liu, Y. Yuan, I. I. Smalyukh, *Nano Lett.* **14**, 4071–4077 (2014).
10. B. Liu *et al.*, *Nat. Commun.* **5**, 3092 (2014).
11. S. K. Sainis, J. W. Merrill, E. R. Dufresne, *Langmuir* **24**, 13334–13337 (2008).
12. A. Yethiraj, A. van Blaaderen, *Nature* **421**, 513–517 (2003).
13. M. F. Hsu, E. R. Dufresne, D. A. Weitz, *Langmuir* **21**, 4881–4887 (2005).
14. T. C. Lubensky, D. Pettey, N. Currier, H. Stark, *Phys. Rev. E* **57**, 610–625 (1998).
15. R. W. Ruhwandl, E. M. Terentjev, *Phys. Rev. E* **55**, 2958–2961 (1997).
16. S. Ramaswamy, R. Nityananda, V. A. Raghunathan, J. Prost, *Mol. Cryst. Liq. Sci. Technol. A* **288**, 175–180 (1996).
17. C. P. Lapointe, T. G. Mason, I. I. Smalyukh, *Science* **326**, 1083–1086 (2009).
18. J. C. Loudet, P. Barois, P. Poulin, *Nature* **407**, 611–613 (2000).
19. A. Nych *et al.*, *Nat. Commun.* **4**, 1489 (2013).
20. F. Wang *et al.*, *Nature* **463**, 1061–1065 (2010).
21. H. Mundoor, I. I. Smalyukh, *Small* **11**, 5572–5580 (2015).
22. Materials and methods are available as supplementary materials on *Science* Online.
23. N. Bogdan, F. Vetrone, G. A. Ozin, J. A. Capobianco, *Nano Lett.* **11**, 835–840 (2011).
24. D. E. Sands, *Introduction to Crystallography* (Dover Publications, 2012).
25. D. B. Conkey, R. P. Trivedi, S. R. P. Pavani, I. I. Smalyukh, R. Piestun, *Opt. Express* **19**, 3835–3842 (2011).
26. C. A. S. Batista, R. G. Larson, N. A. Kotov, *Science* **350**, 1242477 (2015).
27. V. D. Nguyen, S. Faber, Z. Hu, G. H. Wegdam, P. Schall, *Nat. Commun.* **4**, 1584 (2013).
28. R. W. Cahn, *Nature* **413**, 582–583 (2001).
29. R. C. Hayward, D. A. Saville, I. A. Aksay, *Nature* **404**, 56–59 (2000).
30. I. I. Smalyukh, O. D. Lavrentovich, *Phys. Rev. Lett.* **90**, 085503 (2003).

ACKNOWLEDGMENTS

This research was supported by the U.S. Department of Energy, Office of Basic Energy Sciences, Division of Materials Sciences and Engineering, under award ER46921, contract DE-SC0010305 with the University of Colorado–Boulder. We acknowledge the use of electron microscopy facility at the National Institute of Standards and Technology, Boulder, and thank A. Sanders for the help with imaging. We thank P. Ackerman, Q. Liu, T. Lee, and T. Lubensky for discussions.

SUPPLEMENTARY MATERIALS

www.sciencemag.org/content/352/6281/69/suppl/DC1
Materials and Methods
Figs. S1 to S11
Table S1
Movie S1
References (*31*–*39*)

14 December 2015; accepted 26 February 2016
10.1126/science.aaf0801

ELECTROCATALYSIS

Tuning the activity of Pt alloy electrocatalysts by means of the lanthanide contraction

María Escudero-Escribano,[1,2]* Paolo Malacrida,[1] Martin H. Hansen,[3,4] Ulrik G. Vej-Hansen,[1,3] Amado Velázquez-Palenzuela,[1] Vladimir Tripkovic,[3,5] Jakob Schiøtz,[1,3] Jan Rossmeisl,[3,4] Ifan E. L. Stephens,[1,6]* Ib Chorkendorff[1]*

The high platinum loadings required to compensate for the slow kinetics of the oxygen reduction reaction (ORR) impede the widespread uptake of low-temperature fuel cells in automotive vehicles. We have studied the ORR on eight platinum (Pt)–lanthanide and Pt-alkaline earth electrodes, Pt_5M, where M is lanthanum, cerium, samarium, gadolinium, terbium, dysprosium, thulium, or calcium. The materials are among the most active polycrystalline Pt-based catalysts reported, presenting activity enhancement by a factor of 3 to 6 over Pt. The active phase consists of a Pt overlayer formed by acid leaching. The ORR activity versus the bulk lattice parameter follows a high peaked "volcano" relation. We demonstrate how the lanthanide contraction can be used to control strain effects and tune the activity, stability, and reactivity of these materials.

To reduce the Pt loading at the cathode of polymer electrolyte membrane fuel cells (PEMFCs), researchers have intensively studied alloys of Pt with late transition metals such as Ni or Co as oxygen reduction reaction (ORR) electrocatalysts (*1*–*6*). Catalysts exhibiting even greater activity and stability could be designed through the identification of the descriptors that control the performance (*7*–*10*). One single descriptor controls ORR activity, the ΔE_{OH} binding energy, by way of a Sabatier volcano: An ΔE_{OH} ~0.1 eV weaker than Pt(111) yields the optimum value (*11*). Other indirect descriptors related to ΔE_{OH} include the d-band center (*12*), the Pt-Pt

Science

Triclinic nematic colloidal crystals from competing elastic and electrostatic interactions

Haridas Mundoor, Bohdan Senyuk and Ivan I. Smalyukh

Science **352** (6281), 69-73.
DOI: 10.1126/science.aaf0801

Competing forces drive ordering

The power and beauty of liquid crystals come from their tendency to order loosely over long length scales. This ordering can be tweaked using external fields, or via tailored boundary conditions, or embedded objects. Mundoor *et al.* deposited luminescent nanorods into a liquid crystal solvent (see the Perspective by Blanc). This caused a competition between local electrostatic interactions and the elastic ordering of the liquid crystal. The nanorods ordered into a triclinic structure not otherwise attainable. The authors further adjusted the structure using external fields.

Science, this issue p. 69; see also p. 40

Science (print ISSN 0036-8075; online ISSN 1095-9203) is published by the American Association for the Advancement of Science, 1200 New York Avenue NW, Washington, DC 20005. The title *Science* is a registered trademark of AAAS.